Plasmonics (2022) 17:1279–1291
https://doi.org/10.1007/s11468-022-01619-6

A Study of Sensitivity Improved Probe Using Hyperbolic Metamaterial for Optical Fiber SPR (OFSPR)-based Refractive Index Sensor

Sarvesh Kumar Dubey[1] · Anil Kumar[1] · Amritanshu Pandey[2] · Amit Pathak[1] · S. K. Srivastava[1]

Received: 3 February 2022 / Accepted: 25 February 2022 / Published online: 24 March 2022

Abstract
In this work, we theoretically study the plasmonic behavior of Ag and Au with a hyperbolic metamaterial (HMM) and propose a numerical simulation of a D-shaped surface plasmon resonance (SPR)-based refractive index sensor in the near-infrared (NIR) region using the finite element method (FEM). The design of the sensing probe consists of a grating structure of metal (Ag/Au) coated with an alpha-phase molybdenum trioxide (α-MoO_3) HMM layer. The sensing layer of α-MoO_3 over Ag/Au is responsible for the enhanced sensitivity of the optical fiber SPR sensor. This is attributed to the better SPR generation with a metal-dielectric layer. Numerical results show that the proposed sensor is able to detect a refractive index over a large dynamic range of 1.33 to 1.4. With the help of the optimized structure, we achieve maximum sensitivity of 8.31 μm/RIU and 9.89 μm/RIU for the Ag-α-MoO_3- and Au-α-MoO_3-based grating structure, respectively. These results show excellent response in comparison with other reported works.

Keywords Surface plasmon resonance (SPR) · Surface plasmon polariton (SPP) · Hyperbolic metamaterial (HMM) · Finite element method (FEM) · Refractive index (RI)

Introduction

Over the past few decades, various surface plasmon resonance (SPR)-based techniques have been proposed for gas, chemical, and various biosensing applications as well as multifunctional purposes [1–4]. This technique has versatile application due to its portability, detection accuracy, speed, and sensitivity [5], and provides a very simple, real-time, label-free detection method [3]. Conventional SPR sensors (prism-based, etc.) are bulky and costly, whereas optical fiber offers the advantage of portability and compactness [6]. SPR is generated when transverse magnetic (TM) light is incident on the metal–dielectric interface and some absorption of light takes place due to matching of the wave vector of the surface plasmon wave (SPW) and wave vector of incident light. Many types of optical fibers are commercially available for different applications which depend on their operating mode. Electromagnetic waves (emw) of several modes are dominant in multimode optical fiber, while single-mode emw is dominant in single-mode optical fiber. The multimode core is large in diameter in comparison to a single mode core [7, 8]. In the case of simple optical fiber SPR (OFSPR), SPR can be excited in both the single-mode and multimode core in a controlled manner, and their transmission spectrum limits the performance of the sensor. The physical realization of deformed fibers for SPR excitation can be obtained in two simple methods. In the first method, the desired part of the cladding is removed by making a deep cut and polishing one side, and then metal (of certain thickness) is placed over the polished surface. In another method, the tapered optical fiber can be used to fabricate plasmonic metals over its surface. Gold (Au), silver (Ag), copper (Cu), and aluminum (Al) have been demonstrated as noble plasmonic materials which are incorporated into the design of OFSPR sensors. However, chemical instability such as corrosion and oxidation occurs in plasmonic materials other than gold (Au). This can be overcome by coating of other materials such as metal oxides onto plasmonic metals.

✉ S. K. Srivastava
sanjay_itbhu@yahoo.com

[1] Department of Physics, Institute of Science, Banaras Hindu University, Varanasi 221005, India

[2] Department of Electronics Engineering, Indian Institute of Technology-BHU, Varanasi 221005, India

Various studies have reported SPR-based sensors in the near-infrared (NIR) region which have many applications in medicine, environmental sensing, and security purposes [1, 2, 9]. Photonic crystal fiber (PCF) SPR-based sensor techniques have been developed in recent years [10, 11]. Optical fiber sensors with different geometries have been studied, such as tapered geometries [12] and selective cladding removal [13, 14]. An amoeba-faced photonic crystal fiber (A-PCF) structure was reported for the first time in an optical fiber-based biosensor [15]. D-shaped optical fiber is easy to fabricate and can also achieve a large evanescent wave [16]. Various sensing devices have been investigated for refractive index (RI) sensing applications in the NIR, mid-IR, and other regions. Khan et al. [17], studied a D-shaped PCF-based sensor of gold as plasmonic material, achieving maximum wavelength sensitivity of 66.66 µm/RIU [refractive index unit] for a range of 1.36 to 1.39. Huang T. [18] investigated a D-shaped SPR-based PCF RI sensor in a NIR wavelength range using fiber crystal coated with indium tin oxide (ITO). Poole et al. [19] proposed a chemical sensing application using D-shaped optical fiber. Numerous techniques have been proposed for grating-based optical fiber sensor techniques. Compella et al. [20] discussed low-cost strain sensors of unique sensitivity where the sensor was based on fiber Bragg grating (FBG). Many sensing studies have been performed using tapered fiber Bragg grating (TFBG) and long-period fiber grating (LPG) techniques, which have helped to enhance the sensing performance of SPR-based sensors [21].

Several works have been reported on SPR-based sensing using hyperbolic metamaterials (HMMs). Yang et al. [22] performed the synthesis of HMMs using Ag and MgF_2, which was fabricated over D-type plastic optical fibers, and theoretically analyzed the performance using effective medium theory and COMSOL. Hu et al. [23] numerically analyzed HMM-SPR-based sensors and obtained ultrahigh sensitivity of 30 m/RIU, which is very high in comparison to conventional monolayer metallic SPR sensors. Various properties and composition of artificial structured materials have been studied, and applications of metamaterials in devices such as two-dimensional materials, semiconductors, liquid crystals, and superconductors have also been discussed [24]. Cheng et al. [25] numerically investigated the angular and polarization sensitivity of a hexagonal boron nitride (h-BN) array, and also calculated the charge density and corresponding electric field associated with particular responses of strong electric dipole resonance between adjacent h-BN unit cells. Hyperbolic media are characterized by dispersion relation, i.e., permittivity tensors. They have been widely studied for their unique electromagnetic properties [26–28]. This property can be generalized for two-dimensional (2D) materials, called hyperbolic metasurfaces (HMSs). HMSs are nanopatterned photonic structures that can support in-plane hyperbolicity due to guided waves [29, 30]. The α-MoO_3 2D-flake is also a member of the HMM family and possesses an ambient dispersion feature at room temperature. It follows the reststrahlen effect; i.e., in this region, the material of particular crystallographic orientation shows special electromagnetic characteristics, and the resulting radiation experiences strong reflection as shown in Fig. 2a(i). α-MoO_3 is a van der Waals (vdW) crystal that shows naturally in-plane hyperbolic polariton guided modes in a mid-infrared frequency range, and this is a biaxial crystal with three reststrahlen bands, where each reststrahlen band corresponds to a different crystalline axis [31–33], which is shown in Fig. 2. α-MoO_3 has been grown by various synthesis techniques including thermal physical deposition and chemical vapor deposition [32, 34]. Shape-controlled crystalline nanostructures of α-MoO_3 were synthesized by a hydrothermal method without any capping agents [35]. Large-scale, few-layered growth of α-MoO_3 on SiO_2 and Si substrates was carried out using physical vapor deposition [36].

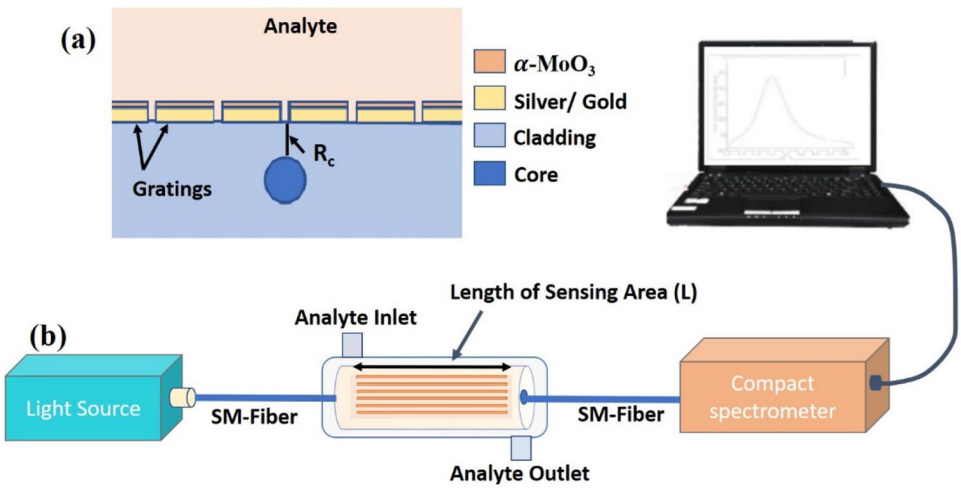

Fig. 1 Schematic diagram of fiber sensor consisting of grating structure of α-MoO_3-coated metal. (**a**) Cross-sectional view of fiber sensor and (**b**) sketch of experimental setup where single-mode (SM) fibers are used

Table 1 Coefficients for core and cladding

Materials	l_1	l_2	l_3	q_1(μm)	q_2(μm)	q_3(μm)
Cladding (pure silica)	0.6961663	0.4079426	0.8974794	0.0684043	0.1162414	9.896161
Core (SiO_2 doped with 3.1% GeO_2)	0.7028554	0.4146307	0.8974540	0.0727723	0.1143085	9.896161

In this work, we theoretically demonstrate the plasmonic behavior of Ag/Au with HMMs and we numerically optimize the performance of D-shaped optical fiber SPR-based sensors, as shown in Fig. 1, where two structurally different sensing media are prepared using Ag-α-MoO_3 and Au-α-MoO_3 nanocomposites in separate configurations. The proposed geometric and performance parameters are optimized using finite element method (FEM)-based software for the optimum application of the proposed sensor. We evaluate the sensitivity of our proposed sensor for various different analyte RI. Our proposed model of the SPR-based sensor achieves maximum sensitivity of 9.89 μm/RIU and 8.31 μm/RIU, revealing good sensing performance as compared to other reported work. The proposed sensor may have a variety of applications in the field of chemical/biological sample diagnostics and other sensing purposes.

Theory

The design of the D-shaped optical fiber SPR (OFSPR)-based RI sensor is shown in Fig. 1. The core is composed of high-dielectric materials in comparison to its cladding, and therefore total internal reflection (TIR) takes place in the core of the optical fiber. The length of the sensing area is assumed to be 1 mm. Further, we have optimized the residual cladding (R_c), grating gap (w_g), and width of gratings (w) by using COMSOL Multiphysics 5.5 FEM-based software. Optical fiber is single-mode in nature, where the core and cladding diameters of the sensors are taken as 9 μm and 125 μm, respectively. Here we assume that a sensing probe of metallic grating structure is deposited at the residual cladding (R_c). The width of the grating (w), gap between gratings (w_g), and grating period ($\wedge = w + w_g$) and number of gratings is kept at 28. A polychromatic light source is assumed to pass through the optical fiber.

Refractive Index of Fiber Core and Cladding For single-mode fiber, the wavelength-dependent core cladding of the RI is calculated by the Sellmeier relation, expressed as [37, 38]

$$n(\lambda) = \left(\frac{l_1\lambda^2}{\lambda^2 - q_1^2} + \frac{l_2\lambda^2}{\lambda^2 - q_2^2} + \frac{l_3\lambda^2}{\lambda^2 - q_3^2} + 1\right)^{\frac{1}{2}} \quad (1)$$

where λ is the operating wavelength (in μm), and l_1, l_2, l_3 and q_1, q_2, q_3 denote the Sellmeier coefficients, whose values are listed in Table 1.

Dispersion Relation of Metal The wavelength-dependent permittivity (ε_m) of dielectric constants of the metals is calculated using the Drude model, given by the relation [37]

$$\varepsilon_m(\lambda) = \varepsilon_\infty - \frac{\lambda^2\lambda_c}{\lambda_p^2\left(\lambda_c + i\lambda_c\right)}, For\ metal\ \varepsilon_\infty = 1 \quad (2)$$

where ε_∞ is the background of the dielectric constant at infinite frequency, and λ_c and λ_P are the collision and plasma wavelength of the metal/metal oxide, respectively (Table 2).

Dispersion Relation of Coating Material The dispersion relation of α-MoO_3 is governed by the generalized form of the Lorentz-Drude relation, which is given as [31]

$$\varepsilon_j = \varepsilon_\infty{}^j\left(1 + \frac{\omega_L^{j^2} + \omega_T^{j^2}}{\omega_T^{j^2} - \omega^2 - i\omega\gamma^j}\right); j \equiv x, y, z \quad (3)$$

ε_j is the principal component of the permittivity tensor, $\varepsilon_\infty{}^j$ is high-frequency dielectric constant, $\omega_L{}^j$ is the longitudinal phonon frequency, $\omega_T{}^j$ is the transverse phonon frequency, and γ^j is the broadening factor of the Lorentzian line shape. The values of phonon frequencies are taken from the literature [40, 41], and $\varepsilon_\infty{}^j$,γ^j are assumed to be a fitting parameter to make the theoretical field distribution match with experimental demonstrations. The electromagnetic properties of α-MoO_3 are shown in Fig. 2.

Expressions for SPR

SPR is an optical absorption effect which describes the complex RI nature of the sensing layer. In the case of SPR, the surface wave vector (k_{sp}) and incident wave vector (k) should be matched. Therefore, the resonance state for SPR excitation is given as [42]

$$k_{sp} = k\sqrt{\frac{\varepsilon_m\varepsilon_s}{\varepsilon_m + \varepsilon_s}}\ where\ k = \frac{2\pi}{\lambda} \quad (4)$$

where for effective excitation of SPs, $\varepsilon_m \gg \varepsilon_s$ and $n_s^2 = \varepsilon_s$,

Table 2 Coefficients for silver and gold

Metal	$\lambda_P(\mu m)$	$\lambda_C(\mu m)$	Reference
Silver	0.14541	17.614	[45]
Gold	0.16826	8.9342	[39]

$$kn_0 Sin\theta = k_{sp} \tag{5}$$

where θ is the incident angle and RI of the core. Again, using Eqs. (4) and (5), the expression can be rewritten as

$$kn_0 Sin\theta k \sqrt{\frac{\varepsilon_m \varepsilon_s}{\varepsilon_m + \varepsilon_s}} \tag{6}$$

where ε_s is the dielectric constant of sensing media such as water or glycerin, and ε_m is the permittivity of metal [43, 44].

Expression for the Transmittance and Confinement Loss Spectrum

T is the transmittance of p-polarized light which is calculated as [45]

$$T = exp[-2k * imag(n_{eff})L] \tag{7}$$

where n_{eff} is the effective RI of the sensing area. The confinement loss of the optical fiber is given as [46, 47]

$$CL\left(\frac{\text{dB}}{\text{cm}}\right) = 8.686k * [imag(n_{eff})]104 \tag{8}$$

Performance Evaluation of Proposed Optical Fiber Sensor

In the present work, the performance parameters of the SPR sensor are mainly dependent on two variables, a shift in resonance wavelength (λ_{res}) and the full width at half minimum (FWHM), which directly correspond to the change in the RI of the sensing medium (n_s) [45, 48–50].

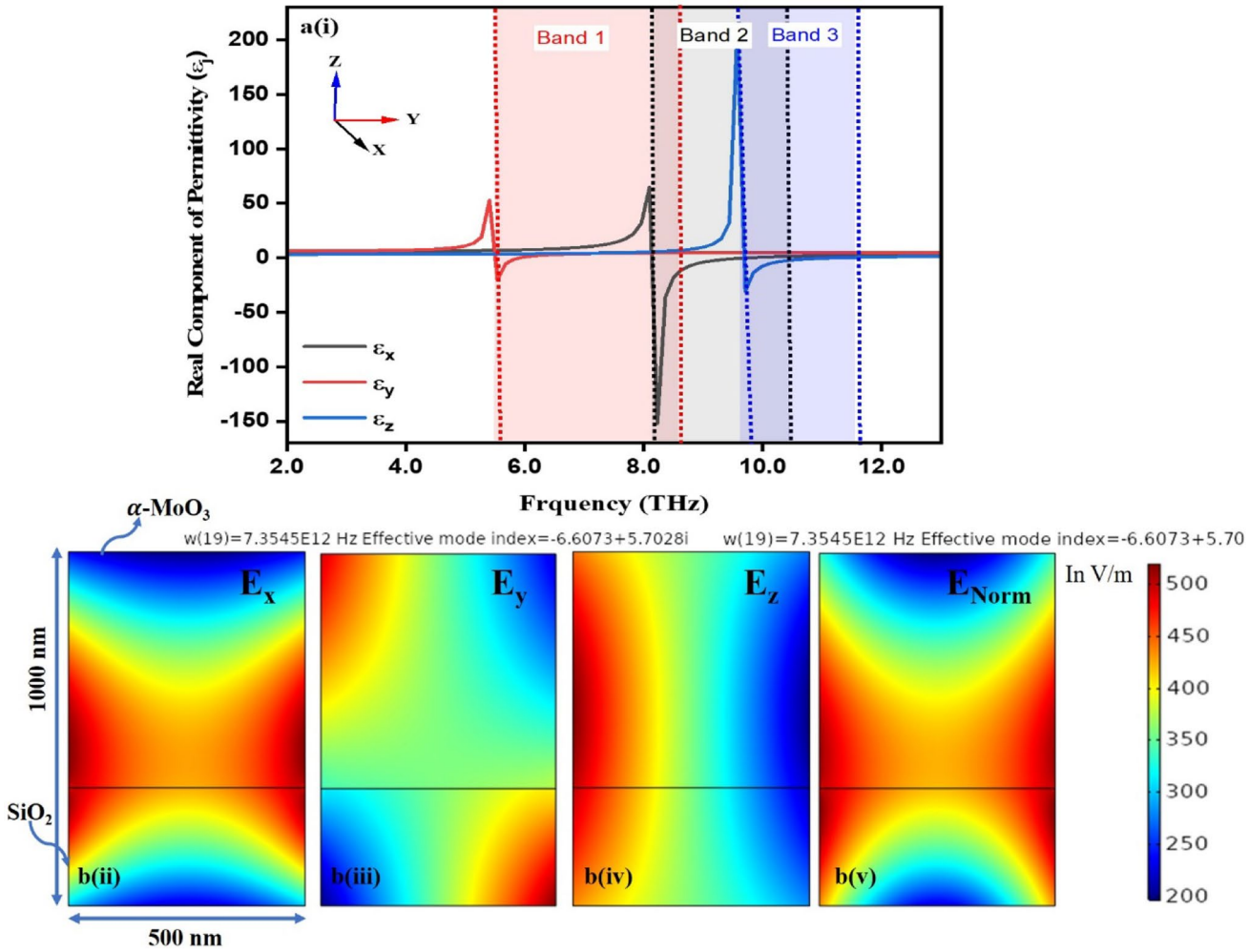

Fig. 2 **a(i)** Electromagnetic (EM) field mode intensity for α-MoO_3 over SiO_2 and dispersion curve vs. linear frequency for all crystallographic axis. (**b**) EM field (in V/m) response of α-MoO_3 over SiO_2 layer. (**ii**), (**iii**), (**iv**), (**v**) EM field mode intensity of the X, Y, Z, and normalized components

Sensitivity In the wavelength interrogation method, sensitivity is obtained from the ratio of the change in resonance wavelength (λ_{res}) to the change in RI of the sensing media (Δn) [48].

$$S = \frac{\Delta \lambda_{res}}{\Delta n} \text{in units of} \left(\frac{\mu m}{RIU} \right),$$

Detection Accuracy (DA) DA is inversely dependent on the FWHM of absorption dip in transmission spectra. The DA indicates the level that a sensor is able to detect with good accuracy [45].

$$DA = \frac{1}{FWHM} (\mu m^{-1})$$

Figure of Merit (FOM) Another crucial parameter used to evaluate the performance of the proposed sensor is the FOM, also known as the quality factor (QF), which is given as [51]

$$FOM = S \times DA = \frac{S}{FWHM} (RIU^{-1})$$

Results and Discussion

In this work, we used FEM-based COMSOL Multiphysics software to evaluate the geometric and performance parameters of our fundamental sensor model. In this study, we employed two-dimensional FEM instead of three-dimensional FEM, as the former requires less simulation time (4–5 h) with the same accuracy. Simulation was carried out by choosing mode analysis with electromagnetic frequency domain (EWFD) physics under wave optics module by applying an impedance boundary condition (IBC) of the same RI, and we take finer meshes (minimum element 0.0181 µm, maximum element size 5.36 µm, and maximum element growth rate 1.25). The dielectric and electromagnetic properties of α-MoO_3 were obtained using Eq. (3) and corresponding Table 3, and are shown in Fig. 2. Further, we optimized the initial parameters of metal/metal oxide thickness, residual cladding, and gratings gap, and the corresponding confinement loss for the primary structure of the proposed sensor is given in Figs. 3, 4, and 5.

Figure 3 shows the electromagnetic field intensity over Ag-α-MoO_3 for an effective mode index, where Ag and α-MoO_3 thickness is kept at 60 nm and 30 nm, respectively. The effective mode corresponds to the particular geometry of plasmonic materials as well as field intensity varying with the change in effective modes. Different types of plasmonic materials, such as Ag, Au, Cu, Al, and transition metal nitrides, exhibit special permittivity characteristics. In this work we theoretically demonstrate the plasmonic behavior of novel plasmonic materials (Ag, Au) with the HMM for a particular operating region.

Figure 4a–d shows the transmission spectra with wavelength for various silver thicknesses, different residual cladding, various grating gaps (w_g), and different grating width (w) values at residual cladding (R_c) at 100 nm, respectively. Here, we have optimized the geometry for optimum performance of our proposed sensor. Various biological and chemical analyte concentrations have RI values ranging from 1.33 to 1.40; therefore, here our interest is in optimizing an SPR-based sensor that can work within this range. Therefore, initially, we assume parameters including analyte RI of 1.35, grating gap of 25 nm, and grating width of 300 nm. Figure 4a shows transmission spectra for different residual claddings (R_c). The first four dips near 550 nm correspond to sensing media consisting of only silver (Ag) gratings of 45 nm, while another three dips near 680 nm correspond to sensing media consisting of Ag-α-MoO_3 and α-MoO_3 of 10 nm for a rough estimation of power absorbance due to SPR. In addition, when a certain thickness of α-MoO_3 is coated over silver, greater SPR occurs and we get a sharper absorption dip in the transmittance curve. Therefore, in our further optimization, we take residual cladding (R_c) at 100 nm to obtain better generation of SPR. In Fig. 4b, we observe that with increasing thickness of Ag, the absorption dip decreases for RI of 1.35, w of 250 nm, and w_g of 20 nm, where, as we increase the thickness of the silver grating, the absorption dip decreases. For Ag thickness of 40 nm, a sharper absorption dip is observed, but if we take this thickness for higher RI (1.39 to 1.40), the transmission curve becomes irregular. Therefore, for our further estimation, it is better to take a silver grating thickness of 60 nm. Figure 4c shows transmission spectra at the different values of gratings gap (w_g)

Table 3 Numerical values of dispersion relation parameters of α-MoO_3

Direction	*X*-axis	*X*-axis	*Y*-axis	*Y*-axis	*Z*-axis	*Z*-axis
	Ref. [32, 33] (cm^{-1})	This work (THz)	Ref. [32, 33] (cm^{-1})	This work (THz)	Ref. [32, 33] (cm^{-1})	This work (THz)
ε_∞	–	4	–	5.2	–	2.4
ω_L	974	29.16	851	25.53	1010	30.12
ω_T	818	24.6	820	16.35	962	28.74
γ	–	0.12	–	0.12	–	0.06

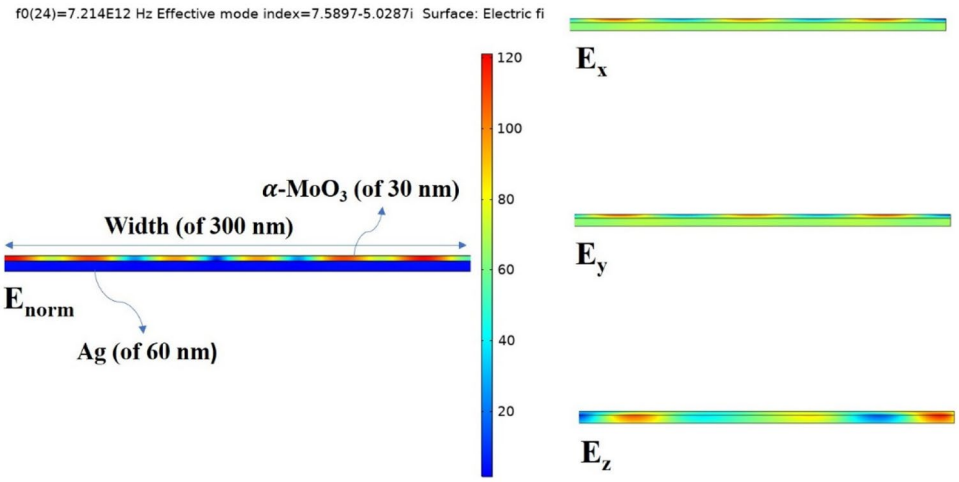

Fig. 3 Normalized and crystallographic axis component of electromagnetic field (in V/m) response of α-MoO_3 over silver layer at a particular mode index

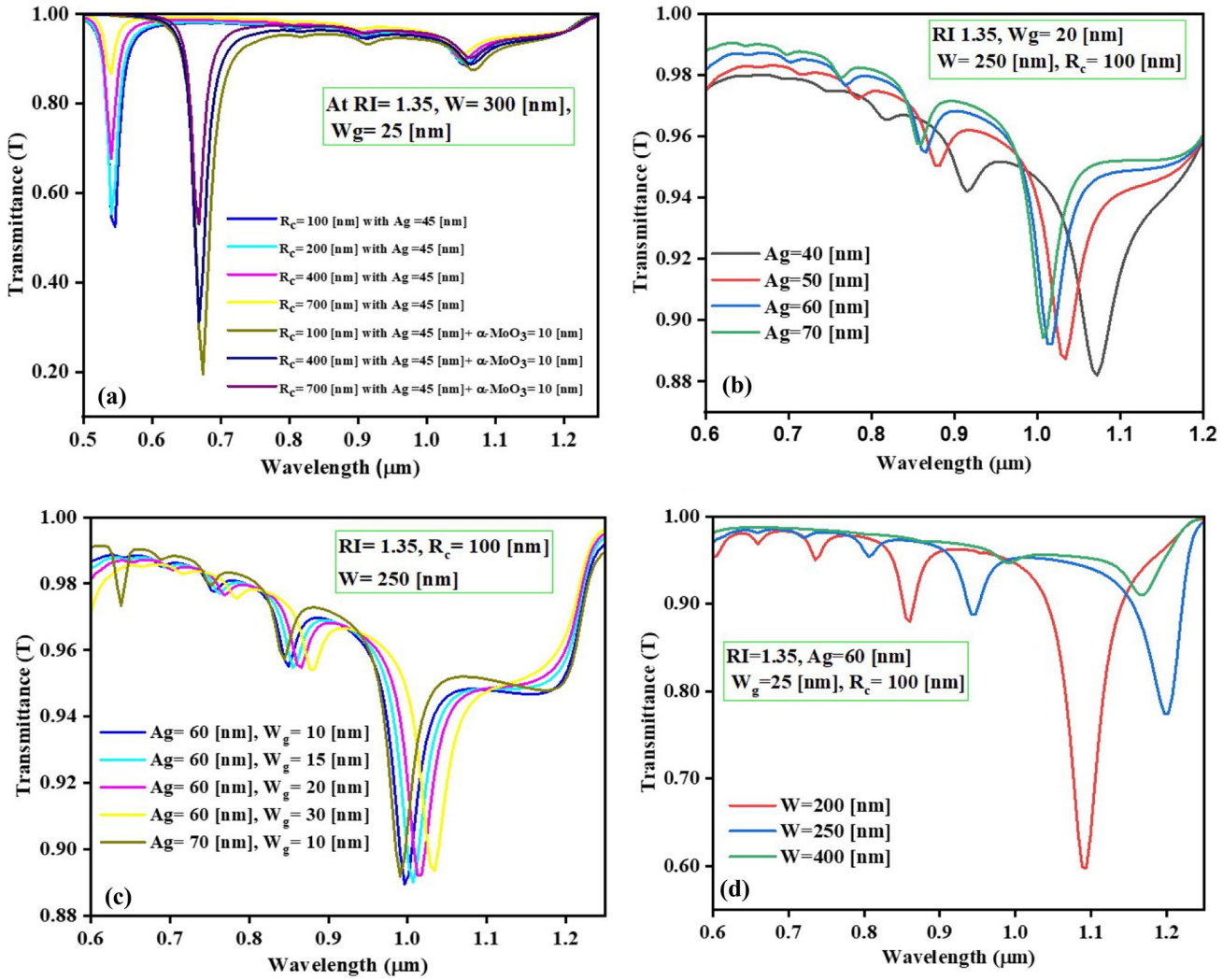

Fig. 4 **(a)** Transmission spectra for different residual cladding thicknesses at w of 250 nm and w_g of 25 nm. **(b)** Transmission spectra for different thickness of silver layer at w_g of 20 nm and w of 250 nm. **(c)** Different silver grating gap (w_g) values at w of 250 nm **(d)** for different grating widths (w) where all RI is 1.35

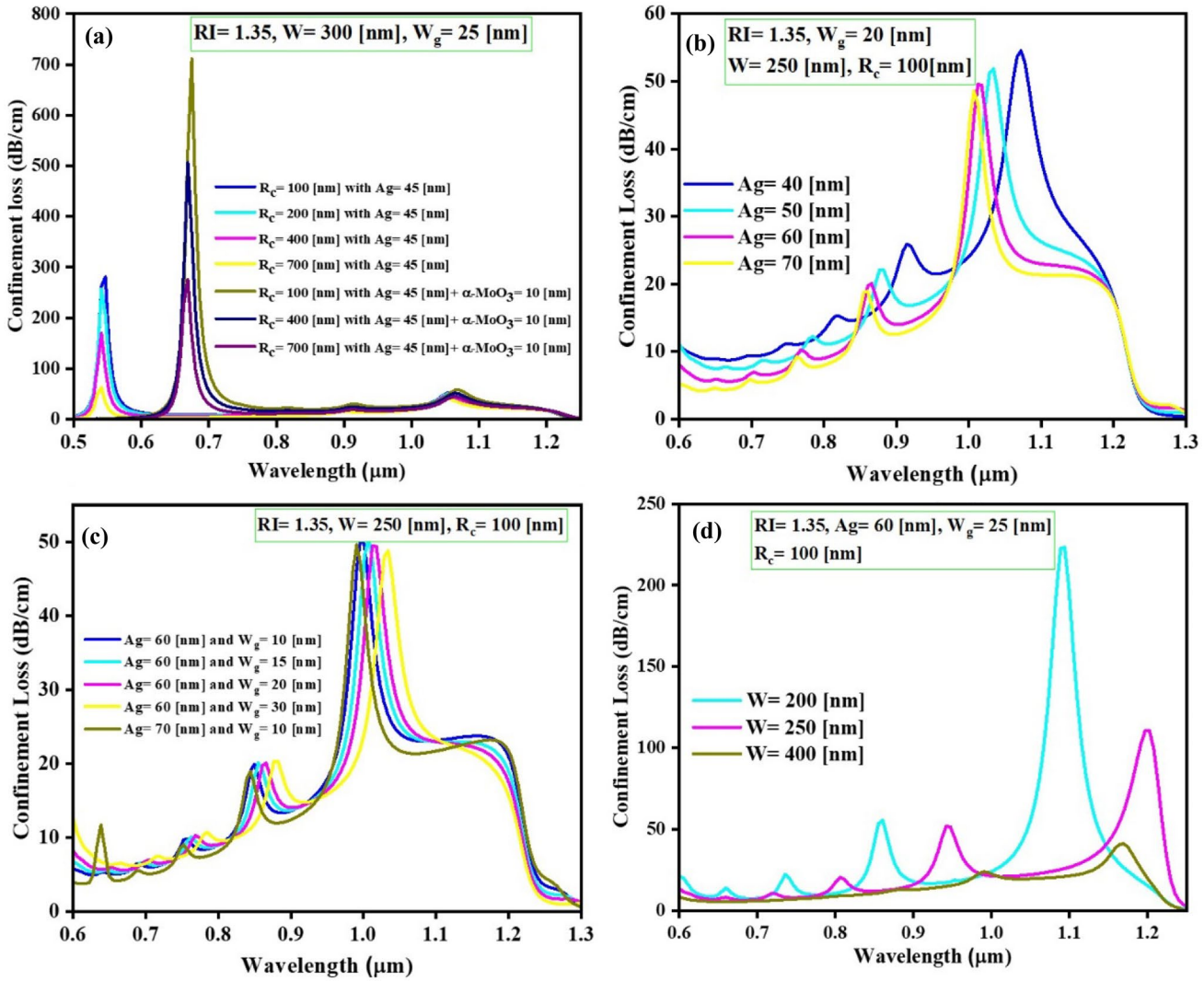

Fig. 5 (**a**) Confinement loss for different residual claddings at particular thicknesses of silver and α-MoO_3 layers at RI = 1.35. (**b**) Confinement loss for different thicknesses of silver layer at RI = 1.35. (**c**) Confinement loss for different value of grating gaps of silver gratings at RI = 1.35. (**d**) Confinement loss for different widths of silver gratings at RI = 1.35, gap of 25 nm

at RI of 1.35 and gratings width (w) of 250 nm. We obtain greater absorption dips for Ag of 60 nm and w_g of 10 nm to 15 nm. The absorption dip decreases slightly as the grating gap increases. Figure 4d shows the transmittance curve for different values of gratings width at Ag of 60 nm, w_g of 25 nm, and RI of 1.35. We observe that a greater absorption dip occurs for w of 200 nm, and the curve becomes irregular for a higher value of gratings width.

Figure 5 shows the confinement loss (CL) vs. wavelength corresponding to Fig. 4. In Fig. 4a, we obtain maximum confinement loss for Ag thickness of 45 nm and residual cladding of 100 nm. Figure 5b shows the confinement loss spectra corresponding to Fig. 4b, and we observe that the CL decreases as the thickness of Ag increases. Figure 5c shows confinement loss for various grating gaps corresponding to Fig. 4c, with the maximum CL observed for Ag thickness of 60 nm and grating gap of 10 nm. Figure 5d shows the CL for various grating widths corresponding to Fig. 4d, where the maximum CL is found for grating width w of 200 nm, with R_c at 100 nm and Ag thickness of 60 nm.

Figure 6 shows the transmittance curve for the distinct value of α-MoO_3 layers over Ag of 60 nm and Au of 50 nm at 1.35 in (a) and (b), respectively. In Fig. 6a we observe that as we increase the thickness of α-MoO_3 with silver of 60 nm, the absorption dip increases and FWHM is minimum; i.e., DA is also better for the higher thickness of α-MoO_3, but we observe some absorption dip irregularity when we set a higher thickness above 28 nm for the α-MoO_3 layer. In Fig. 6b, as we increase the thickness of α-MoO_3 over the gold layer of 50 nm, the absorption dip increases as

we increase the thickness of α-MoO_3 up to 30 nm, but there is sharp irregularity above 30 nm, and for higher values of RI, FWHM is greater; i.e., DA is less good in comparison to Ag-α-MoO_3. In Fig. 6c, at α-MoO_3 of 15 nm, as we increase the thicknesses of the silver grating, the absorption dip decreases, but a very slight shift occurs in the resonance wavelength. In Fig. 6d, at α-MoO_3 of 15 nm, as the thickness of gold grating increases, the absorption dip decreases, and a slight shift in the resonance wavelength occurs.

Figure 7 shows the SPR electric field and surface plasmon polariton (SPP) mode at corresponding transmittance spectra. Figure 7a, b i, ii shows Ag-α-MoO_3, with Ag at 60 nm and α-MoO_3 at 15 nm. Figure 7c, d, iii, iv shows Au-α-MoO_3, with Au at 50 nm and α-MoO_3 at 10 nm. The SPR field response and transmittance curve are illustrated via the FEM-based software COMSOL. We can see that the core mode and SPP mode occur at 0.7651 μm and 0.7593 μm for Ag-α-MoO_3 and Au-α-MoO_3, respectively. At this point, most of the electric field in the fiber core is transferred to the sensing area of Ag-α-MoO_3 and Au-α-MoO_3. As a result, some power loss inside the optical fiber is observed, which is called absorption dip. Therefore, the electric field strength of SPR increases over the grating surface. Along with this, we can see in Fig. 7ii, iv that the α-MoO_3 layer also enhances the SPR field intensity at the sensing area.

Figure 8 shows the transmission spectra for different external RI values at Ag-α-MoO_3 and Au-α-MoO_3 in (a) and (b), respectively. In Fig. 8a, for Ag-α-MoO_3, where Ag thickness is 60 nm and α-MoO_3 is 15 nm, the absorption dips increase with increasing RI values up to 1.4, where FWHM is minimum. In Fig. 8b, for Au-α-MoO_3, where Au thickness is maintained at 50 nm and α-MoO_3 is 10 nm, the

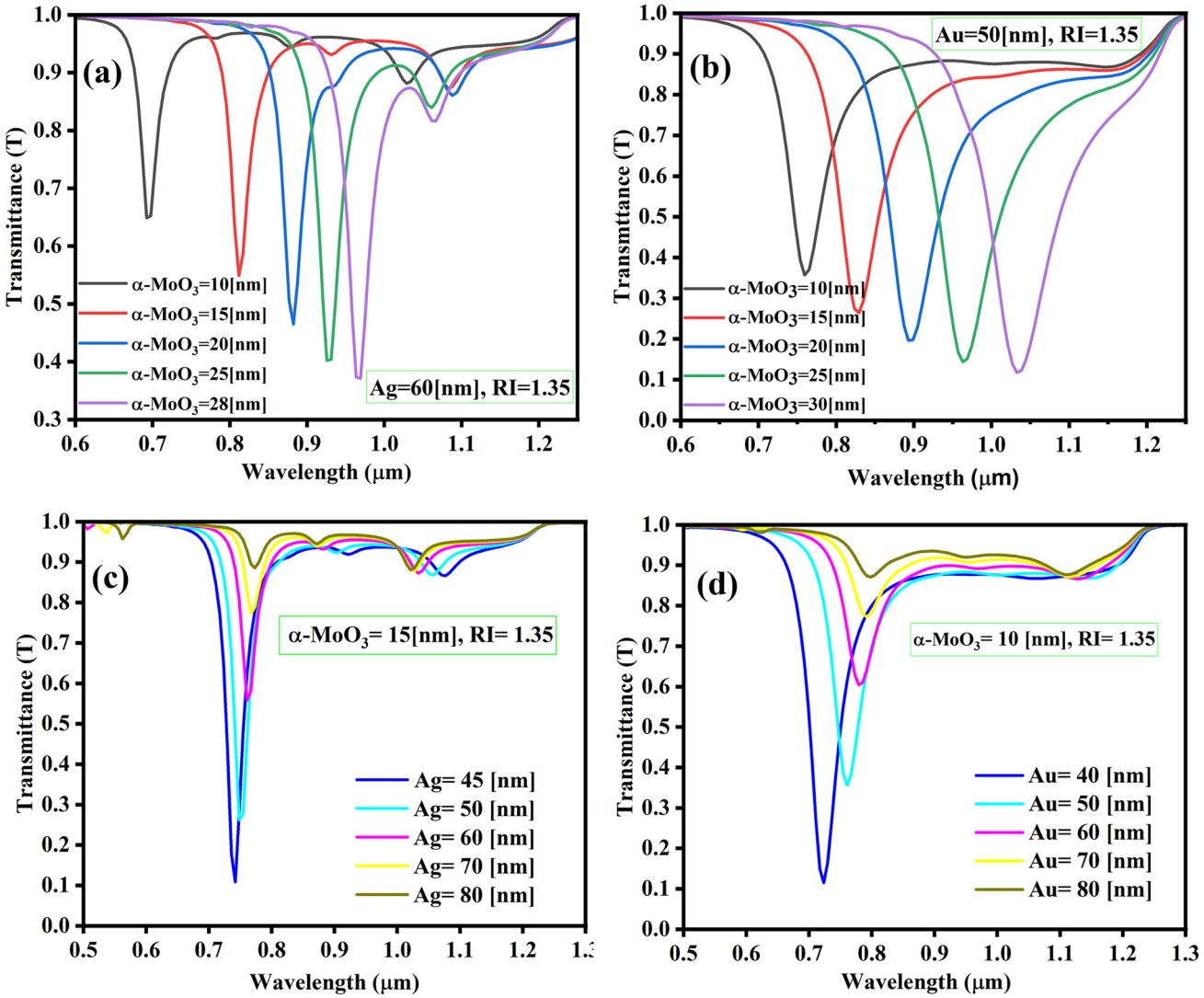

Fig. 6 (**a**), (**b**) Transmission curve for various thicknesses of α-MoO_3 over silver layer of 60 nm thickness and over gold layer of 50 nm thickness, respectively. (**c**), (**d**) Transmission spectra for various thicknesses of silver and gold gratings with fixed thickness of α-MoO_3, respectively

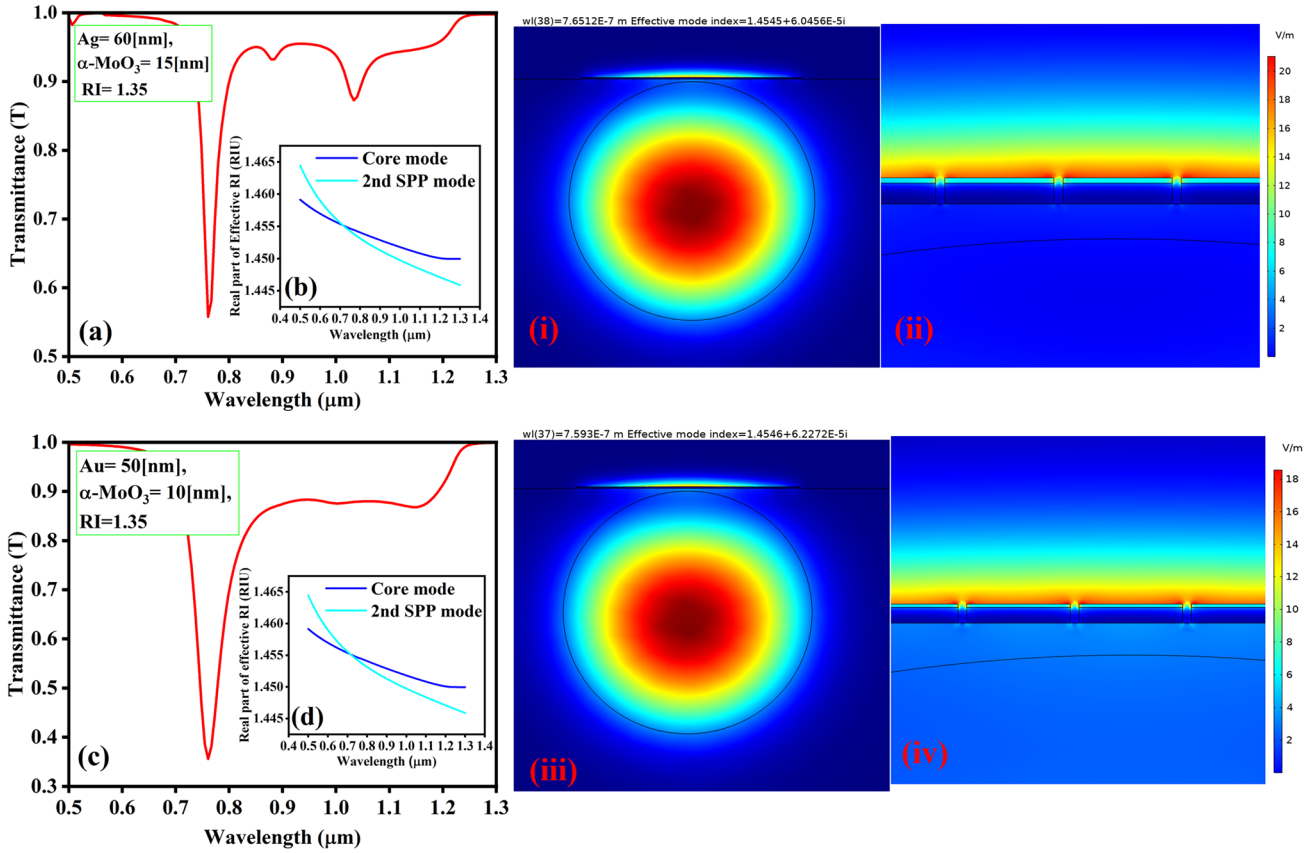

Fig. 7 (**a**), (**b**) Transmission spectra for silver grating of 60 nm thickness with α-MoO_3 layer of 15 nm thickness. (**b**) SPP and core mode corresponding to (**a**). (**i**, **ii**) EM field of SPR mode corresponding to both (**a**) and (**b**). (**c**) Transmission spectra for gold grating of thickness 50 nm with α-MoO_3 of thickness 10 nm. (**d**) SPP and core mode corresponding to (**c**). (**iii**,**iv**) EM field of SPR mode corresponding to both (**c**) and (**d**)

absorption dips increase as the value of the RI increases up to 1.4, where the FWHM is much greater, i.e., DA is less in comparison to the Ag-α-MoO_3 configuration.

Figure 9 shows the relationship between the RI and resonance wavelength at different thicknesses of α-MoO_3 layers over Ag and Au, respectively. In Fig. 9a, where silver

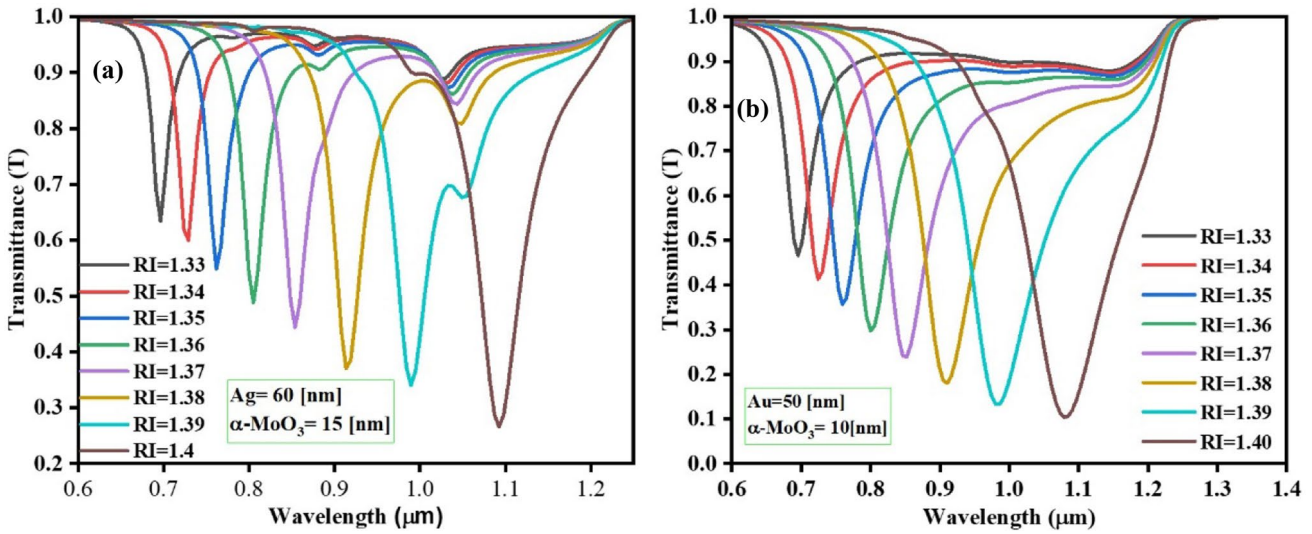

Fig. 8 (**a**) Transmission spectra for different refractive indices where silver grating thickness is 60 nm and α-MoO_3 layer thickness is 15 nm. (**b**) Transmission spectra for different refractive indices where gold grating thickness is 50 nm and α-MoO_3 layer thickness is 10 nm

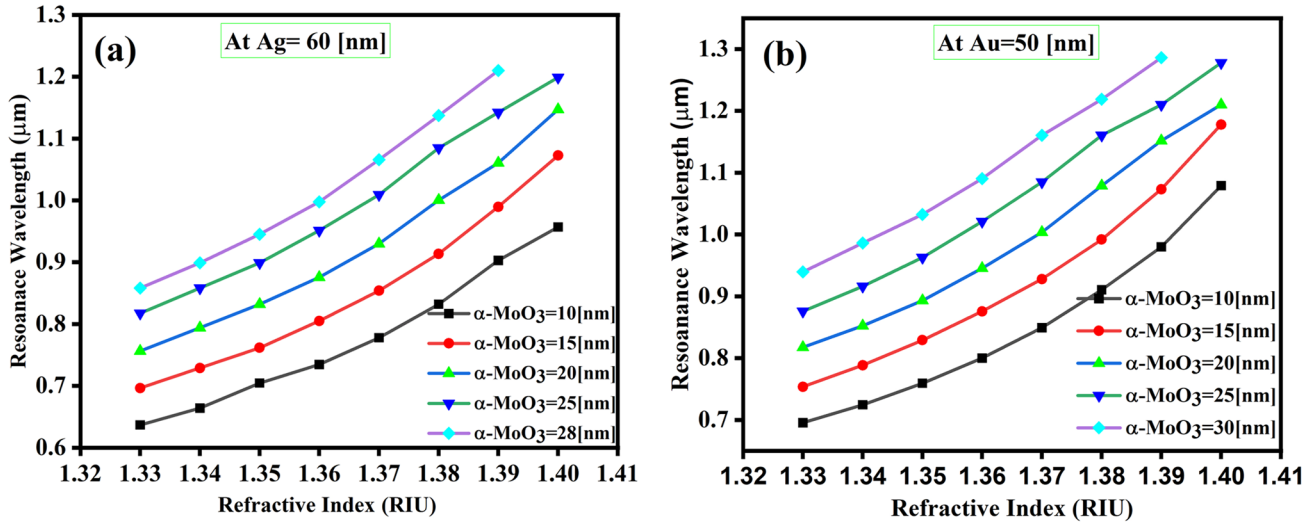

Fig. 9 (**a**) Curve of resonance wavelength vs. RI of medium for different thicknesses of α-MoO_3 layer with silver thickness of 60 nm. (**b**) Curve of resonance wavelength vs. RI of medium for different thicknesses of α-MoO_3 layer with gold thickness of 50 nm

thickness is 60 nm, for various thicknesses of the coating layer α-MoO_3, the resonance wavelength increases as the external RI increases. There is an increase in λ_{res} from 1.36 RIU to 1.39 RIU. In Fig. 9b, where gold thickness is 50 nm, for various thicknesses of coating layer α-MoO_3, λ_{res} increases with increasing RI. We observe an absorption dip irregularity at 1.4 RIU for 28 nm of α-MoO_3 over Au of 50 nm.

Figure 10 shows the sensitivity curve with different thicknesses of α-MoO_3. In this figure we evaluate the effect of the thickness of the metal oxide layer on the sensitivity of the proposed model. In Fig. 10a, for Ag-α-MoO_3, we measured the sensitivity for various thicknesses of α-MoO_3. The sensitivity values for α-MoO_3 thickness of 10 nm, 15 nm, 20 nm, 25 nm, and 28 nm are 5.42 μm/RIU, 8.31 μm/RIU, 8.64 μm /RIU, 5.67 μm/RIU, and 3.08 μm/RIU, respectively. For Ag of 60 nm and α-MoO_3 of 15 nm and 20 nm, it shows the best sensitivity of 8.31 μm/RIU and 8.64 μm/RIU and FOM of 296.99 RIU^{-1} and 235.04 RIU^{-1} for 15 nm and 20 nm thickness of α-MoO_3, respectively, which is tabulated in Table 4. In Fig. 10b, for the Au-α-MoO_3 sensing probe, we evaluated the effect on sensitivity with the change in α-MoO_3 thickness. The sensitivity values for α-MoO_3 thickness of 10 nm, 15 nm, 20 nm, 25 nm, and 28 nm are 9.89 μm/RIU, 10.46 μm

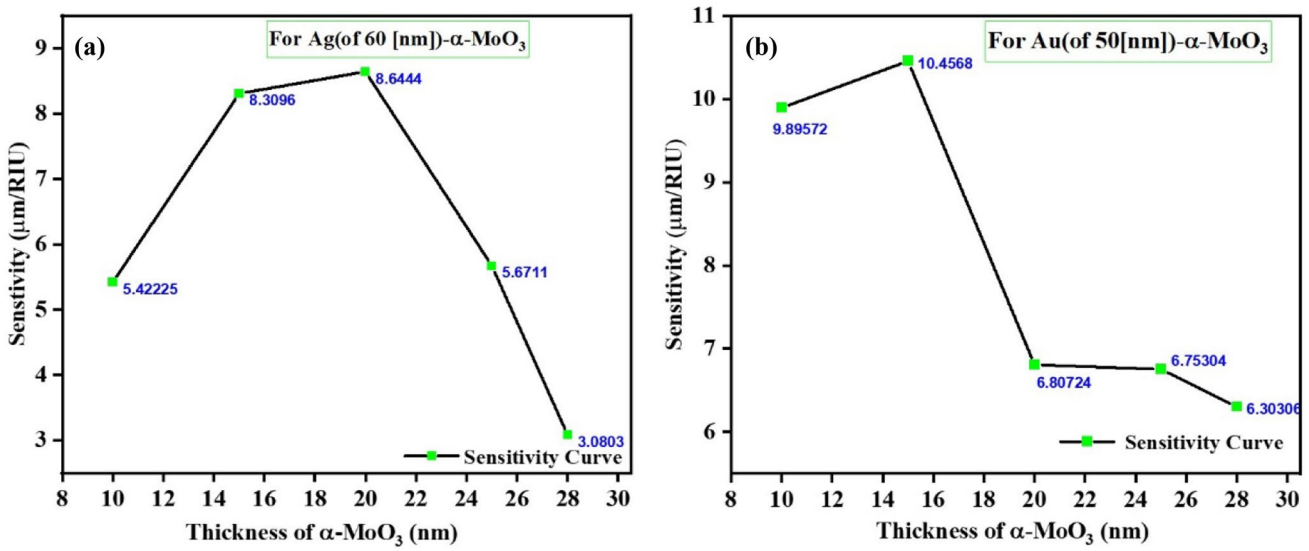

Fig. 10 (**a**) Sensitivity curve for different thicknesses of α-MoO_3 with silver grating thickness of 60 nm. (**b**) Sensitivity curve for different thicknesses of α-MoO_3 with gold grating thickness of 50 nm

Table 4 Performance parameters at different thicknesses of α-MoO_3 over silver

Ag of 60 (nm) and α-MoO_3 thickness (*nm*)	$\Delta\lambda_{res}$(μm)	Δ*n*(RIU)	Sensitivity (μm/RIU)	DA (μm^{-1}) at RI = 1.39	FOM (RIU^{-1}) at RI = 1.39
10	0.0542	0.01	5.42	38.9177	210.93
15	0.0831	0.01	8.31	35.7389	296.99
20	0.0864	0.01	8.64	27.2034	235.04
25	0.0567	0.01	5.67	29.1002	164.99
28	0.0308	0.01	3.08	27.1514	83.63

Table 5 Performance parameters at different thicknesses of α-MoO_3 over gold

Au of 50 (nm) and α-MoO_3 thickness (nm)	$\Delta\lambda_{res}$(μm)	Δn(RIU)	Sensitivity (μm/RIU)	DA (μm^{-1}) at RI = 1.39	FOM (RIU^{-1}) at RI = 1.39
10	0.09895	0.01	9.89	15.63	154.58
15	0.10457	0.01	10.46	14.01	146.52
20	0.06807	0.01	6.81	13.13	89.42
25	0.06530	0.01	6.75	10.64	71.82
28	0.06303	0.01	6.31	9.73	61.39

/RIU, 6.81 μm/RIU, 6.75 μm/RIU, and 6.31 μm/RIU, respectively. For Au of 50 nm with α-MoO_3 thickness of 10 nm and 15 nm, we obtain good sensitivity of 9.89 μm/RIU and 10.46 μm/RIU, and FOM of 154.58 RIU^{-1} and 146.52 RIU^{-1}, respectively, which is given in Table 5.

Conclusion

In this work, we have optimized a D-shaped OFSPR-based RI sensor which consists of a grating structure of Ag-α-MoO_3 and Au-α-MoO_3 in a separate configuration. We studied the effect of the thickness of the metal oxide layer of α-MoO_3 HMM over the silver and gold layer. We also studied the variation in SPR electric field intensity on grating surfaces. In the Ag-α-MoO_3-based sensor, the thickness of Ag and α-MoO_3 was kept at 60 nm and 15 nm, respectively, and for the Au-α-MoO_3-based sensor, the thickness of Au and α-MoO_3 was taken to be 50 nm and 10 nm, respectively. In both cases, the number of gratings was 28. The simulation demonstrated that in the case of the Ag-α-MoO_3 configuration, the maximum and minimum sensitivity were 8.64 μm/RIU and 3.08 μm/RIU, respectively, whereas in the case of the Au-α-MoO_3 configuration, we obtained maximum and minimum sensitivity of 10.46 μm/RIU and 6.31 μm/RIU, respectively. The performance of the proposed sensor was compared with other reported devices, as listed in Table 6. Based on the results, the D-shaped optical fiber SPR-based sensor is an affordable technique that has great potential for application in chemical and environmental diagnostic and sensing fields.

Table 6 Comparison with other reported works

Sensor type	Materials	RI range	Maximum sensitivity (μm/RIU)	Reference
D-type PCF	Silica-TiO_2-Ag	1.29 to 1.39	135	[52]
D-type PCF	Au	1.36 to 1.38	3.34	[53]
D-type PCF	Au	1.18 to 1.36	20	[54]
D-type fiber	Ag + GO	1.30 to 1.34	0.83	[55]
D-type fiber	Au	1.35 to 1.43	0.91	[56]
D-type fiber	G + ITO	1.33 to 1.35	5.70	[57]
D-type fiber	Ag-TiO_2, Ag-SnO_2	1.325 to 1.355	15.31, 9.81	[58]
D-type fiber	Ag-α-Fe_2O_3	1.33 to 1.39	6.40	[45]
D-type fiber	Ag-α-MoO_3	1.33 to 1.40	8.31	Present work
D-type fiber	Au-α-MoO_3	1.33 to 1.40	9.89	Present work

Author Contributions Sarvesh K. Dubey proposed the idea and performed analytical and numerical simulation, and writing the initial and final draft. Anil Kumar edited the manuscript. Amritanshu Pandey helped in simulation work. All authors reviewed and analyzed the manuscript. S. K. Srivastava supervised and Amit Pathak co-supervised this project.

Funding Sarvesh K. Dubey and Anil Kumar are thankful to CSIR-UGC (Govt. of India) for providing fellowships. S. K. Srivastava acknowledges IOE (Institute of Eminence) scheme for faculty for providing financial support.

Availability of Data and Material The data is confidential.

Software Availability COMSOL Multiphysics id- apandey.ece@iitbhu.ac.in, Dr. Amritanshu Pandey Department of Electronics Engineering, Indian Institute of Technology-BHU.

Declarations

Ethics Approval No human subjects were involved in this study. It is an original study, and currently, this manuscript is not submitted for review to any other journal. This will not be submitted elsewhere before a decision is made by this journal.

Consent to Participate No human subjects were involved in this study.

Conflict of Interest The authors declare no competing interests.

References

1. Ouyang Q, Zeng S, Jiang L, Hong L, Xu G, Dinh X-Q, Qian J, He S, Qu J, Coquet P (2016) Sensitivity enhancement of transition metal dichalcogenides/silicon nanostructure-based surface plasmon resonance biosensor. Sci Rep 6:1–13
2. Tamersit K, Djeffal F (2016) Double-gate graphene nanoribbon field-effect transistor for DNA and gas sensing applications: simulation study and sensitivity analysis. IEEE Sens J 16:4180–4191
3. Nguyen HH, Park J, Kang S, Kim M (2015) Surface plasmon resonance: a versatile technique for biosensor applications. Sensors 15:10481–10510
4. Kumar A, Kumar A, Kushwaha AS, Dubey SK, Srivastava SK (2022) A comparative study of different types of sandwiched structures of SPR biosensor for sensitive detection of ssDNA. Photonics Nanostruct Fundam Appl 48:100984
5. Zeng Y, Hu R, Wang L, Gu D, He J, Wu S-Y, Ho H-P, Li X, Qu J, Gao BZ, Shao Y (2017) Recent advances in surface plasmon resonance imaging: detection speed, sensitivity, and portability. Nanophotonics 6:1017–1030
6. Kumar R (2019) High sensitivity micro/nano singlemode-multimode-singlemode fibre sensors, University of Northumbria at Newcastle (United Kingdom)
7. Addanki S, Amiri IS, Yupapin P (2018) Review of optical fibers-introduction and applications in fiber lasers. Results in Physics 10:743–750
8. Liu X (2019) Evolution of fiber-optic transmission and networking toward the 5G era. iScience 22:489–506
9. Piliarik M, Homola J, Manıková Z, Čtyroký J (2003) Surface plasmon resonance sensor based on a single-mode polarization-maintaining optical fiber. Sens Actuators, B Chem 90:236–242
10. Rifat AA, Ahmed K, Asaduzzaman S, Paul BK, Ahmed R (2019) Development of photonic crystal fiber-based gas/chemical sensors, in: Computational photonic sensors, Springer 287–317
11. Hossen MN, Ferdous M, Khalek MA, Chakma S, Paul BK, Ahmed K (2018) Design and analysis of biosensor based on surface plasmon resonance. Sensing and bio-sensing research 21:1–6
12. Dıez A, Andres M, Cruz J (2001) In-line fiber-optic sensors based on the excitation of surface plasma modes in metal-coated tapered fibers. Sens Actuators, B Chem 73:95–99
13. Kurihara K, Ohkawa H, Iwasaki Y, Tobita T, Niwa O, Suzuki K (2001) Microscale fiber-optic SPR sensors based on NSOM technology, in: Micro Total Analysis Systems 2001, Springer 353–354
14. Jorgenson RC, Yee SS (1993) A fiber-optic chemical sensor based on surface plasmon resonance. Sens Actuators, B Chem 12:213–220
15. Jabin MA, Luo Y, Peng G-D, Rana MJ, Ahmed K, Nguyen TK, Paul BK, Dhasarathan V (2020) Design and fabrication of amoeba faced photonic crystal fiber for biosensing application. Sensors Actuators A Phys 313:112204
16. Hoo Y, Jin W, Ho HL, Wang D, Windeler RS (2002) Evanescent-wave gas sensing using microstructure fiber. Opt Eng 41:8–9
17. Khan MS, Ahmed K, Hossain MN, Paul BK, Nguyen TK, Dhasarathan V (2020) Exploring refractive index sensor using gold coated D-shaped photonic crystal fiber for biosensing applications. Optik 202:163649
18. Huang T (2017) Highly Sensitive spr sensor based on D-shaped photonic crystal fiber coated with indium tin oxide at near-infrared wavelength. Plasmonics 12:583–588
19. Poole ZL, Ohodnicki P, Chen R, Lin Y, Chen KP (2014) Engineering metal oxide nanostructures for the fiber optic sensor platform. Opt Express 22:2665–2674
20. Campanella CE, Cuccovillo A, Campanella C, Yurt A, Passaro VMN (2018) Fibre bragg grating based strain sensors: review of technology and applications. Sensors 18:3115
21. Sharma AK, Marques C (2019) Design and performance perspectives on fiber optic sensors with plasmonic nanostructures and gratings: A review. IEEE Sens J 19:7168–7178
22. Yang W, Gao J, Li Z, Li C, Cheng Y, Huo Y, Jiang S, Jiang M (2021) High performance D-type plastic fiber SPR sensor based on a hyperbolic metamaterial composed of Ag/MgF 2. J Mater Chem C 9:13647–13658
23. Hu S, Shi W, Chen Y, Chen Y, Liu G-S, Chen L, Luo Y, Chen Z (2022) Dispersion management for hyperbolic-metamaterials based surface plasmon resonance sensor towards extremely high sensitivity. Optica Publishing Group 40(3):887–893
24. Xiao S, Wang T, Liu T, Zhou C, Jiang X, Zhang J (2020) Active metamaterials and metadevices: a review. J Phys D Appl Phys 53:503002
25. Cheng L, Wang T, Jiang X, Yan X, Xiao S (2017) Polarization and angular sensibility in the natural hyperbolic hexagonal boron nitride arrays. J Phys D Appl Phys 50:435104
26. Smith D, Schurig D (2003) Electromagnetic wave propagation in media with indefinite permittivity and permeability tensors. Phys Rev Lett 90:077405
27. Poddubny A, Iorsh I, Belov P, Kivshar Y (2013) Hyperbolic metamaterials. Nat Photonics 7 (12), 948–957 In Nature Publishing Group, a division of Macmillan Publishers Limited
28. Drachev VP, Podolskiy VA, Kildishev AV (2013) Hyperbolic metamaterials: new physics behind a classical problem. Opt Express 21:15048–15064
29. Kildishev AV, Boltasseva A, Shalaev VM (2013) Planar photonics with metasurfaces. Science 339
30. Yu N, Capasso F (2014) Flat optics with designer metasurfaces. Nat Mater 13:139–150

31. Zheng Z, Xu N, Oscurato SL, Tamagnone M, Sun F, Jiang Y, Ke Y, Chen J, Huang W, Wilson WL, Ambrosio A, Deng S, Chen H (2019) A mid-infrared biaxial hyperbolic van der Waals crystal. Sci Adv 5:eaav8690
32. Zheng Z, Chen J, Wang Y, Wang X, Chen X, Liu P, Xu J, Xie W, Chen H, Deng S (2018) Highly confined and tunable hyperbolic phonon polaritons in van der Waals semiconducting transition metal oxides. Adv Mater 30:1705318
33. Li P, Dolado I, Alfaro-Mozaz FJ, Casanova F, Hueso LE, Liu S, Edgar JH, Nikitin AY, Vélez S, Hillenbrand R (2018) Infrared hyperbolic metasurface based on nanostructured van der Waals materials. Science 359:892–896
34. Saenz GA, Kaul AB (2020) Nanosheets of MoOx crystallites synthesized via chemical vapor deposition and its potential in bolometric applications. Surf Coat Technol 382:125031
35. Sharma R, Jha R, Sarkar A, Sharma AK, Sharma D, Bhushan M, Bhardwaj R (2020) Controlled growth of α-MoO3 nanostructures with enhanced optical and electrochemical properties without capping agents. Ceram Int 46:23084–23097
36. Wang Y, Du X, Wang J, Su M, Wan X, Meng H, Xie W, Xu J, Liu P (2017) Growth of Large-Scale, Large-Size, Few-Layered α-MoO3 on SiO2 and its photoresponse mechanism. ACS Appl Mater Interfaces 9:5543–5549
37. Shamala K, Murthy L, Rao KN (2004) Studies on tin oxide films prepared by electron beam evaporation and spray pyrolysis methods. Bull Mater Sci 27:295–301
38. DeVore JR (1951) Refractive indices of rutile and sphalerite. JOSA 41:416–419
39. Verma RK, Sharma AK, Gupta B (2008) Surface plasmon resonance based tapered fiber optic sensor with different taper profiles. Opt Commun 281:1486–1491
40. Zheng Z, Chen J, Wang Y, Wang X, Chen X, Liu P, Xu JB, Chen H, Deng S, Xu N (2018) Phonon polaritons: highly confined and tunable hyperbolic phonon polaritons in van der waals semiconducting transition metal oxides (Adv. Mater. 13/2018). Adv Mat 30
41. Ma W, Alonso-González P, Li S, Nikitin AY, Yuan J, Martín-Sánchez J, Taboada-Gutiérrez J, Amenabar I, Li P, Vélez S, Tollan C, Dai Z, Zhang Y, Sriram S, Kalantar-Zadeh K, Lee ST, Hillenbrand R, Bao Q (2018) In-plane anisotropic and ultra-low-loss polaritons in a natural van der Waals crystal. Nature 562:557–562
42. Cao J, Sun Y, Kong Y, Qian W (2019) The sensitivity of grating-based spr sensors with wavelength interrogation. Sensors 19:405
43. Sharma AK, Jha R, Gupta B (2007) Fiber-optic sensors based on surface plasmon resonance: a comprehensive review. IEEE Sens J 7:1118–1129
44. Sathukarn A, Jia yi C, Boonruang S, Horprathum M, Tantiwanichapan K, Prasertsuk K, Thanapirom C, Kusolthossakul W, Kasamsook K (2020) The simulation of a surface plasmon resonance metallic grating for maximizing thz sensitivity in refractive index sensor application. Int J Optics 2020:3138725
45. Kadhim RA, Yuan L, Xu H, Wu J, Wang Z (2020) Highly sensitive D-shaped optical fiber surface plasmon resonance refractive index sensor based on Ag-α-Fe 2 O 3 grating. IEEE Sens J 20:9816–9824
46. Sharma AK, Gupta B (2007) On the performance of different bimetallic combinations in surface plasmon resonance based fiber optic sensors. J Appl Phys 101:093111
47. Monfared YE, Kurylyk BL, Dasog M (2022) Highly sensitive plasmonic fiber-optic sensors using group IV transition metal nitrides: a numerical investigation. Plasmonics
48. Salari M, Askari H (2013) Theoretical investigation of absorption and sensitivity of nano-plasmonic fiber optic sensors. Opt Laser Technol 48:315–325
49. Sharma AK, Gupta BD (2005) Fibre-optic sensor based on surface plasmon resonance with Ag–Au alloy nanoparticle films. Nanotechnology 17:124–131
50. Sharma AK, Gupta BD (2007) Comparison of performance parameters of conventional and nano-plasmonic fiber optic sensors. Plasmonics 2:51–54
51. Rhodes C, Cerruti M, Efremenko A, Losego M, Aspnes D, Maria J-P, Franzen S (2008) Dependence of plasmon polaritons on the thickness of indium tin oxide thin films. J Appl Phys 103:093108
52. Noman AA, Haque E, Hossain MA, Hai NH, Namihira Y, Ahmed F (2020) Sensitivity Enhancement of modified D-shaped microchannel pcf-based surface plasmon resonance sensor. Sensors 20:6049
53. Lu J, Li Y, Han Y, Liu Y, Gao J (2018) D-shaped photonic crystal fiber plasmonic refractive index sensor based on gold grating. Appl Opt 57:5268–5272
54. Haque E, Hossain MA, Ahmed F, Namihira Y (2018) Surface plasmon resonance sensor based on modified D-shaped photonic crystal fiber for wider range of refractive index detection. IEEE Sens J 18:8287–8293
55. Amiri IS, Alwi SAK, Raya SA, Zainuddin NAAM, Rohizat NS, Rajan MM, Zakaria R (2019) Graphene oxide effect on improvement of silver surface plasmon resonance D-shaped optical fiber sensor. J Opt Commun
56. Ying Y, Wang J, Hu N, Xu K, Sun L, Si G (2020) Determination of refractive index using surface plasmon resonance (SPR) and rigorous coupled wave analysis (RCWA) with a D-shaped optical fiber and a nano-gold grating. Instrum Sci Technol 48:376–385
57. Patnaik A, Senthilnathan K, Jha R (2015) Graphene-based conducting metal oxide coated D-shaped optical fiber SPR sensor. IEEE Photonics Technol Lett 27:2437–2440
58. Dubey SK, Kumar A, Kumar A, Pathak A, Srivastava S (2021) A study of highly sensitive D-shaped optical fiber surface plasmon resonance based refractive index sensor using grating structures of Ag-TiO2 and Ag-SnO2. Optik 168527